Near Surface Geophysics, 2018, **16**, 238-256 doi: 10.3997/1873-0604.2018005

Different techniques for the assessment of geoelectrical data errors to improve the electrical images obtained at an industrial plant

Patricia Martinelli[1,2], Ana Osella[1,2*], Matias de la Vega[1,2] and Alejandro Pinio[1,3]

[1] *Departamento de Física, Facultad de Ciencias Exactas y Naturales, Universidad de Buenos Aires, Buenos Aires, Argentina.*
[2] *Instituto de Física de Buenos Aires (IFIBA), CONICET-Universidad de Buenos Aires, Buenos Aires, Argentina*
[3] *On a fellowship from Agencia Nacional de Promoción Científica y Tecnológica (ANPCyT), Argentina*

Received August 2017, revision accepted April 2018.

ABSTRACT

The objective of this work was to characterise the bases of columns belonging to an industrial plant. We had to design a proper methodology for characterising these structures, in a place with limited available space and time for the deployment of sensors, and with other environmental constraints, such as high electromagnetic noise level, soil vibrations due to operating machines, and complex soil composition. In particular, the floor had a stainless steel cover about 1-cm thick, below which there was first a layer of concrete about 30-cm thick and then clay material used to absorb the oils of the machines. Finally, there was the natural soil on which the column bases stood.

Given these characteristics, we performed dipole–dipole geoelectric profiles. Holes were drilled through the metallic cover and the concrete layer, with fixed spacings, to insert the electrodes. Because of this and the space and time restrictions, only one profile could be performed for each column. Since we knew that the data could have high noise levels and other errors negatively impacting the data quality, and also because there was a limitation to the length of the profiles, we optimised the measurement configuration by jointly using several electrode apertures, to ensure the best possible resolution and sufficient penetration depth. To obtain adequate error estimations, we performed direct and reciprocal measurements. As an alternative technique, we also carried out a second set of direct measurements, after removing and reinstalling the electrodes.

Then, for each profile, we performed 2D inversions of the three datasets separately, without considering data errors. Besides, we inverted the datasets obtained by combining the first direct and the reciprocal measurements, and the first and second direct measurements, considering the two obtained error estimates. In addition, numerical simulations were made, combining direct 3D modelling with 2D inversions. To analyse the results, we took into account the knowledge we had in advance about the main characteristics of the structures.

The first conclusion obtained is that, at least for this type of structures, inverting each dataset without considering data errors provided more realistic images. However, although the best results were obtained by inverting without considering errors, it was still fundamental to have different sets of data, for evaluating the reliability of the images and for discarding possible spurious artefacts. This is especially important in environmentally complex urban sites, where errors could be particularly high. Finally, through the numerical simulations, a more rigorous interpretation could be made, and also, the effect of data errors in the quality of the images could be assessed.

Key words: Urban geophysics, Electrical resistivity tomography, Error assessment, 3D forward modelling

INTRODUCTION

Geophysical methods are increasingly being applied in complex urban sites. They are used, for example, to characterise archeological remains, tunnels, gas station subsurface contamination, and other subsurface structures (e.g., Leucci and Negri 2006; Eppelbaum 2011). These methods have also been applied as an aid to civil engineering projects to investigate the subsurface for maintenance of large structures such as bridges or buildings

---

[*] osella@df.uba.ar

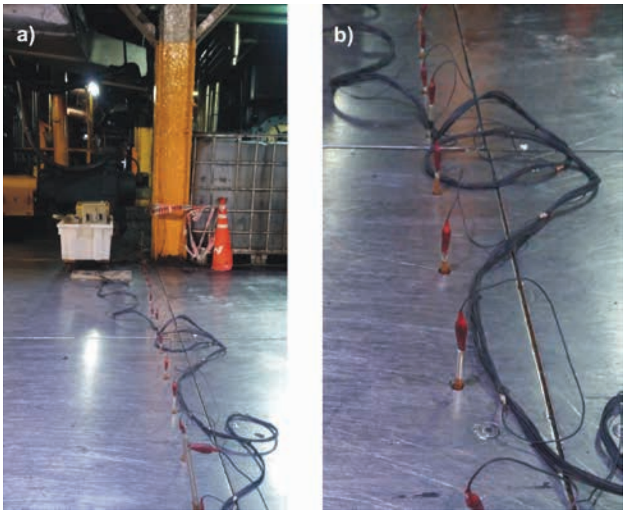

Figure 1 (a) Photo of the interior of the industrial plant showing one of the columns, the stainless steel floor cover, and the electrodes and cables deployment. (b) Zoomed-in view of the electrodes and cables.

(e.g., Karhunen *et al*. 2010, Arjwech *et al*. 2013, Niederleithinger, Abraham and Mooney 2015).

In this paper, we present a geophysical study made at an industrial plant located in a highly populated zone. The goal of this study was to characterise the subsurface bases of 12 columns of a sector of the plant (Figure 1a). This was required prior to a planned extension of the plant. It was known that the bases consisted of square cuboids of concrete, laterally centred with respect to the columns; however, their dimensions and depths were poorly documented. Of particular interest was the determination of the lateral extent of these cuboids.

Environmental noise in cities (electric, electromagnetic, vibrations, etc.) affects the geophysical measurements. Besides, the access to the survey areas is often physically and/or temporarily limited by other uses, which generally restrict the amount of data that can be acquired (Papadopoulos *et al.* 2009; Osella *et al.* 2015). Also, the structures are usually embedded in upper layers with intricate heterogeneities caused by urban development (Drahor 2011). All these factors decrease the quality of the data and the resolution of the obtained images, reducing the capability of identifying and characterising the targets.

In our specific study, we had to face the considerable electromagnetic noise contamination typical of industrial plants and also a high level of vibrations due to the machinery, which was always in operation. Besides, the available measuring time was short, and the free space for the field measurements was relatively scarce. Additionally, the site presented other complex features for the application of geophysical methods. The floor had a stainless steel cover about 1-cm thick. Underneath, there was a layer of concrete about 30-cm thick, followed by clay material used to absorb the oils of the machines. Finally, there was the natural soil where the column bases stood. For these reasons, we had to disregard, for example, seismic, GPR, and electromagnetic induction methods, or ultrasonic echo testing techniques, successful in other urban environments (e.g., Eppelbaum 2011; Tsokas *et al.* 2011; Bonomo *et al.* 2012). Instead, we selected the geoelectrical method, also called electrical resistivity tomography (ERT), for it is less affected by the kind of problems described (e.g., Dahlin and Zhou 2004; Martorana *et al.* 2009; Szalai, Novák and Szarka 2011; Osella *et al.* 2015). Nevertheless, we had to design appropriate measurement strategies to minimise the effects of these difficult characteristics and improve the obtained results.

As the floor cover was metallic, capacitive contacts could not be used (Dabas *et al*. 2000). Thus, holes had to be drilled through the metal cover and the concrete layer to place the electrodes, which introduced additional effects to be considered. The presence of the machinery negatively affected the subsoil and the electrode/soil contact in two main ways: by the leakage of oils that directly modified the electrical conductivity, and due to the vibrations that contributed to reduce the repeatability of the measurements, especially where the natural soil or the clay filling material was less compact. The importance of these effects, which reduced data quality, depended on the characteristics of the different machines and their proximity to the columns. Overall, we expected a heterogeneous background, instead of a more or less uniform one, and variable error levels, which could be very high in the most critical zones. Taking into account the spatial constraints in the site, only one line of holes was prepared for each column and base, centred with respect to their location. For each line, data were acquired with the dipole–dipole electrode configuration and then inverted to obtain 2D electrical images of the subsoil. This array was selected because it normally has good sensitivity to lateral resistivity changes in the subsoil. In addition, among the traditional arrays, it is the one that best allows the detection of localised parallelepiped structures (such as the vertical sections of the studied bases) in noisy environments (Szalai et al. 2013).

In general, the inversion of geoelectrical data is usually made without taking into account data errors, since accurately estimating these errors is particularly difficult (Loke *et al*. 2013). Although the equipment reports the standard deviations of the measurements, which account for the random errors, quite frequently, the data can present systematic errors of equal or even greater magnitude than the random ones (e.g., Zhou and Dahlin 2003; Loke *et al*. 2013). Among the most common sources of systematic errors are deficiencies of electrode contacts with the ground and electrode polarisation. In our particular case, where some of these errors were expected to be high, not considering these errors could lead to unreliable results.

The standard way to do error estimations that include the non-random effects is to perform reciprocal measurements (Parasnis 1988; Park and Van 1991). For the dipole–dipole configuration, this procedure usually provides accurate results using the same acquisition settings as for the direct measurements. However, for other common arrays, such as Wenner-α and Schlumberger, special care must be taken in determining the correct acquisition parameters for the reciprocal measurements; otherwise, the errors may be overestimated due to the large distance between the potential electrodes, in comparison with the distance between the current electrodes.

We investigated the possibility of estimating data errors reasonably through carrying out a second set of direct measurements after removing and reinstalling the electrodes. This is not the same as repeating the direct measurements without removing the electrodes and, in our case, provided different results than that procedure, precisely due to the complex characteristics of the subsoil and the conditions of data acquisition, as previously described. In this paper, we analyse the effectiveness of this alternative approach. As reciprocal measurements were also made, we first compare the two obtained error estimates, then we compare the results of the separate 2D inversions of the data corresponding to the two direct and the reciprocal measurements which were carried out without considering data errors, and finally we obtain the 2D images when each of these error estimates is included in the inversion process.

In the assessment of the quality of the inversion results, our main criterion was to estimate the similarity of the models with what we knew about the general characteristics of the targets, instead of prioritising the convergence errors (e.g., see Szalai *et al.* 2014). Although the analysis using this criterion is more difficult, it is better to apply when it is possible (e.g., analogue modelling, field test measurements, or the situation discussed here), because comparing convergence errors may be misleading, which will be discussed later. While convergence errors compare derivative data (measured and calculated data), similarity directly compares the obtained model to what it is actually known.

For most columns, a good representation of the subsoil resistivity was obtained; yet, even in these cases, the interpretation of some features of the observed anomalies was not clear. Therefore, to improve the interpretation, we performed a numerical simulation study, in order to find an explanation of the possible origin of those features. We proposed schematic 3D models, representative of the structures present in the studied site, including the columns and their bases. We calculated the synthetic dipole–dipole geoelectric responses of these 3D models, for lines located in positions similar to those of the survey profiles, and then performed 2D inversions of these responses. The comparison between the images obtained from the acquired and synthetic data allowed for a reliable interpretation at each column.

METHODOLOGY FOR DATA ACQUISITION AND INVERSION

We prospected a total of 12 columns, similar to the one shown in Figure 1a. As previously described, the floor at the site had a stainless steel cover about 1-cm thick, below which there was approximately 30 cm of concrete. To perform the geoelectrical measurements, stainless steel electrodes of 8 mm in diameter and 45 cm in length were used. These electrodes were inserted in holes of 13 mm in diameter, drilled across these layers prior to the survey, until they reached the clay filling material and/or the natural soil. The body of the electrodes was coated with insulating material to prevent current leakage to the concrete and/or the metallic floor covering. One line of holes was made for each column, centred with respect to the column and separated from it by 10 cm. The distance between the holes along each line was 25 cm and was selected considering the available information about the approximate dimensions and depths of the column bases. The body of the electrodes was coated with insulating material, to prevent current leakage to the concrete and/or the metallic floor covering (Figure 1(a,b)).

For the reasons formerly explained, we used the dipole–dipole electrode configuration. The linear space available for the lines of holes — each one corresponding to one profile — was between 8 m and 10 m. Given this constraint and the expected high levels of noise and other sources of errors in the data, the acquisition parameters had to be optimised to achieve the highest possible resolutions and penetration depths. For this, measurements with different electrode spacings, a = 0.5 m, 1 m, 1.5 m, 2 m, and 2.5 m, were carried out along the profiles, with a station step of 0.25 m. The corresponding maximum dipole separation factors were, respectively, n = 8, 6, 3, 2, and 1.

For each profile, we first performed direct measurements named D1 and then reciprocal ones named R1. After that, the electrodes were removed and relocated at the same holes, and a new set of direct measurements, D2, was carried out. We did not use water or any other element, in order to avoid adding further alterations to the soil; in fact, the problem was not the soil resistivity. Because of this, all these data were acquired with a Saris 500 instrument (Scintrex) in a manual acquisition mode, to have strict control of the active electrodes. In this way, we could rapidly and efficiently detect problems in the contact of the electrodes with the ground, which was improved when possible by increasing the depth of the embedding.

We generated datasets D1 & R1 and D1 & D2 by combining, for each data point, the apparent resistivities ρ_a(D1), ρ_a(R1) and ρ_a(D2) obtained respectively from the measurements D1, R1, and D2, as follows:

$$\rho_a(D1\,\&\,R1) = [\rho_a(D1) + \rho_a(R1)]/2, \tag{1}$$

$$\rho_a(D1\,\&\,D2) = [\rho_a(D1) + \rho_a(D2)]/2. \tag{2}$$

The error estimates arising from the comparison among the data D1 and R1, and D1 and D2 were, respectively, calculated as:

$$\Delta\rho_a(D1\,\&\,R1) = |\rho_a(D1) - \rho_a(R1)|/2, \tag{3}$$

$$\Delta\rho_a(D1\,\&\,D2) = |\rho_a(D1) - \rho_a(D2)|/2. \tag{4}$$

Equation (3) corresponds to the standard procedure for obtaining data error estimates, whereas equation (4) corresponds to the approach investigated here.

The respective relative errors were obtained as follows:

$$\varepsilon(D1\,\&\,R1) = \Delta\rho_a(D1\,\&\,R1)/\rho_a(D1\,\&\,R1), \tag{5}$$

$$\varepsilon(D1\,\&\,D2) = \Delta\rho_a(D1\,\&\,D2)/\rho_a(D1\,\&\,D2). \tag{6}$$

The data were inverted using the code Res2Dinvx64, version 4.05, by Geotomo Software (Loke and Barker 1996a), to obtain models of the electrical resistivity of the subsoil below each line. In these models, the vertical coordinate z is negative downwards, and $z = 0$ m corresponds to the top of the metallic floor covering. The datasets D1, R1, and D2 were inverted separately without considering the data errors (which is the most common practice), whereas for the data D1 & R1 and D1 & D2, the error estimates in equations (3) and (4) were respectively used. In every case, the data of all the electrode spacings used were inverted together. For some profiles, topographical corrections were applied, since variations of up to 30 cm were observed in the depth of the contact point of each electrode with the soil.

In addition to the usual least-square (L2 norm) inversion, the program also offers a robust inversion option in which the absolute values (L1 norm) of the data misfit are minimised (Loke, Acworth and Dahlin 2003). We selected this robust data constraint option for all the inversions, because it allows reducing the effect of data errors in the resulting models. Regarding the model constraints, the square (L2 norm) or the absolute (L1 norm) changes in the model resistivity values can be minimised. As it is well known, the first procedure generates models with smooth resistivity variations. On the other hand, the robust model constraint tends to produce "blocky" models, with sharp interfaces between regions with approximately constant resistivity. We selected this last option, because the described blocky models were more consistent with the expected subsurface structures. Table 1 lists the values of the main parameters used for the inversions.

In the following section, we present the results obtained for three profiles, named 1, 2, and 3, corresponding to three different columns. They are representative of the diverse target and soil features found in the study. They also correspond to different data error levels and hence exemplify the effects of these differences on the inversion results. The lengths of the selected profiles are 8 m, 9.75 m, and 8.25 m, respectively.

RESULTS

Profile 1

As a first example, Figure 2(a–c) shows, respectively, the apparent resistivity pseudosections of the data D1, R1, and D2, corresponding to Profile 1. In this case, the column had a square section of 0.27 m on each side and was centred at $x = 4$ m. The pseudosections of the two relative error estimates for these data, calculated from equations 5 and 6, are shown, respectively, in Figure 3(a,b). The errors obtained with the standard approach (Figure 3a) were lower than 8%, with a mean value of 2.9%. This indicates that the effects caused by poor electrode contact, elec-

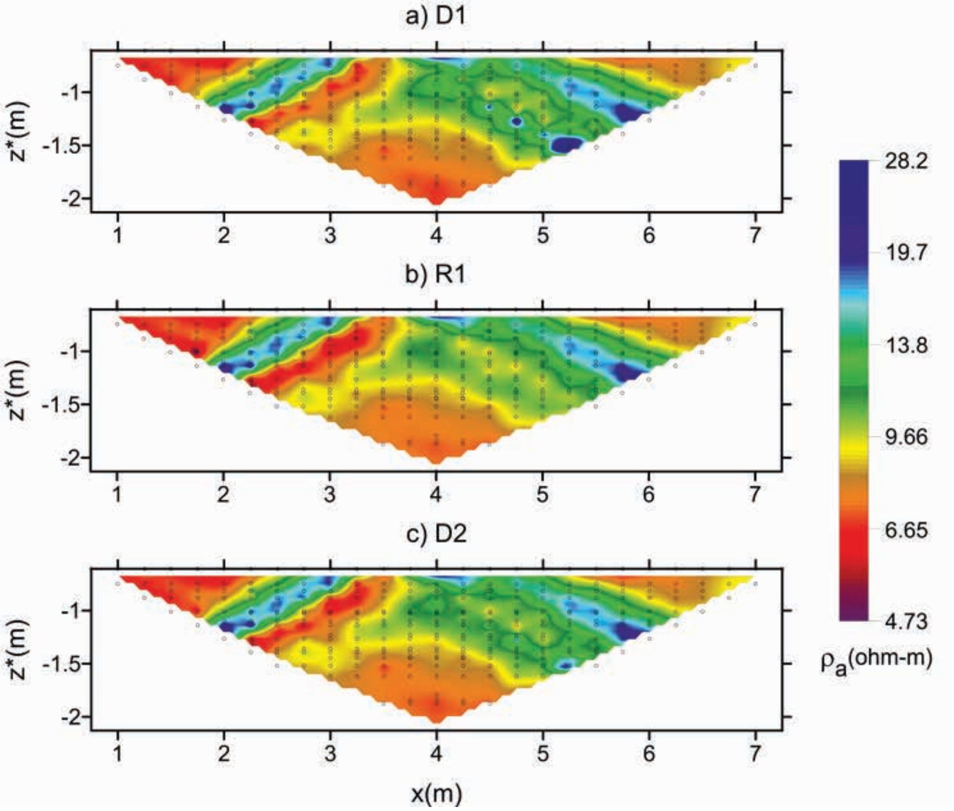

Figure 2 Apparent resistivity pseudosections corresponding to Profile 1 for (a) the first set of direct measurements (data D1), (b) the reciprocal measurements (data R1), and (c) the second set of direct measurements, performed after reinstalling the electrodes (data D2). Z* denotes the median depth of investigation (after Edwards 1977).

trode polarisation, or other noise sources were relatively low for this profile. The alternative error estimates (Figure 3b), in general, exhibit similar distribution as the standard ones, although their maximum and mean values are somewhat smaller, 6% and 1.8%, respectively.

The results of the 2D inversions of the data D1, R1, and D2, performed without providing to the program any information about data errors, are shown, respectively, in Figure 4(a–c). These inversions had good convergence. In the seventh iteration, the mean absolute errors of the fittings were less than 8.2%. The three models obtained display similar anomalies, laterally centred at the position of the column. A resistive structure (anomaly A) is observed between x = 2.7 m and 5.3 m and depths 0.8–1.6 m, approximately, which contains two more resistive areas, with resistivity of about 100 Ωm, localised almost symmetrically with respect to the column. Surrounded by this structure and the upper resistive cover material (anomaly B), we find a very conductive body (0.8 Ωm), approximately 0.8- to 1-m wide (anomaly C). Both the geometry of these anomalies and the fact that their contours appear well defined are consistent with what was expected, considering the previous knowledge about the general features of the targets.

Outside the described central zone, an area with average resistivity of the order of 10 Ωm is observed, with some resistivity variations that account for local inhomogeneities. This area can be associated to the host layer, which was altered by scattered materials and by the presence of oils and other chemical products leaked from the machines.

Then, we inverted the data D1 & R1 obtained from equation (1), using the data error estimations defined by equation (3), and the data D1 & D2 obtained from equation (2), using the error estimations by equation (4). The resulting 2D models are shown in Figure 5(a,b), respectively.

In the case of the inversion of the data D1 & R1, convergence was already reached in iteration 5, with an error of 2.7%. Even though this convergence error is lower than the ones obtained for the inversions of D1 and R1 (7.8% and 5.7%, respectively), the quality of the obtained image (Figure 5a) is inferior. The same anomalies as in the models shown in Figure 4(a,b) are observed, but their shape is worse delineated and their resistivity contrasts are lower.

For the data D1 & D2 (Figure 5b), the inversion error at iteration 5 was 6.4%. Despite the different data error estimates considered, a result analogous to the case of D1 & R1 was obtained, with only some slight differences in the maximum and minimum resistivities.

Another relevant point is that the images obtained from the inversion of the data D2 and D1 & D2 are, respectively, similar to the ones obtained from R1 and D1 & R1. This indicates that regarding the inversion results, at least for this profile where data errors were low, the acquisition of a second set of direct measurements was as useful as performing reciprocal measurements. In addition, the fact that the same anomalies are present in all the models, although with some differences, confirms that they correspond to real subsurface structures and are not to spurious effects.

Table 1 Values of the main inversion parameters.

Initial damping factor	0.15–0.35
Minimum damping factor	0.02
Line search option	Always
Minimum change in RMS error for line search	0.5%
Convergence limit for the relative change in the	
RMS error between two iterations	2 to 5%
RMS convergence limit	2 to 5%
Vertical to horizontal flatness filter ratio	1
Number of nodes between adjacent electrodes	4
Type of Jacobian matrix calculation	Gauss–Newton
Data constraint	Robust
Cut-off factor for robust data constraint	0.05
Model constraint	Robust
Cut-off factor for robust model constraint	0.005
Extended model	No
Reduce the effect of side blocks	Slight
Forward modelling method	Finite elements
Type of mesh	Finest
Width of blocks	Normal
Blocks have the same width	Yes
Logarithm of apparent resistivity	Yes
Type of reference resistivity	Average
Model refinement	Half-width cells
Type of optimisation method	Gauss–Newton

Profile 2

As a second example, we present the results corresponding to Profile 2, which was located in the sector of the industrial plant with the worst conditions for data acquisition, mainly due to the proximity of the machinery and the abundance of contaminant oils in the soil. This column had a square section of 0.42 m on each side and was centred at x = 4.8 m. Figure 6(a–c) shows, respectively, the apparent resistivity pseudosections corresponding to the data D1, R1, and D2. The pseudosections of the standard (equation (5)) and alternative (equation (6)) relative error estimations for these data are shown, respectively, in Figure 7(a,b). As can be appreciated from Figure 7a, data errors were on the whole much greater than in the previous case (Figure 3). Their mean and maximum values were, respectively, 18% and 70%. This was a direct consequence of the adverse measurement conditions mentioned before. The most problematic part was the zone located

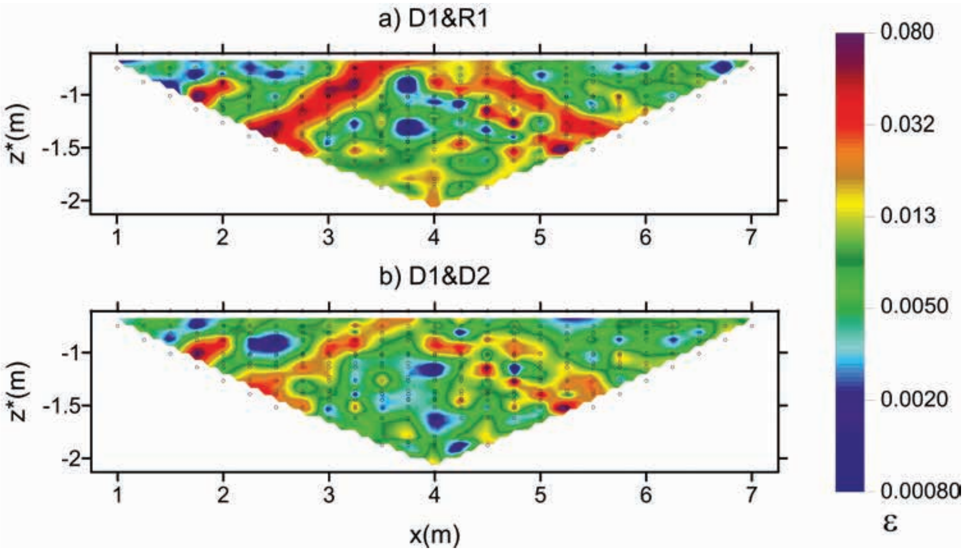

Figure 3 Pseudosections of unitless relative errors, ε, for Profile 1, calculated (a) from the data D1 and R1 through equation (5) and (b) from the data D1 and D2 through equation (6). Z* denotes the median depth of investigation.

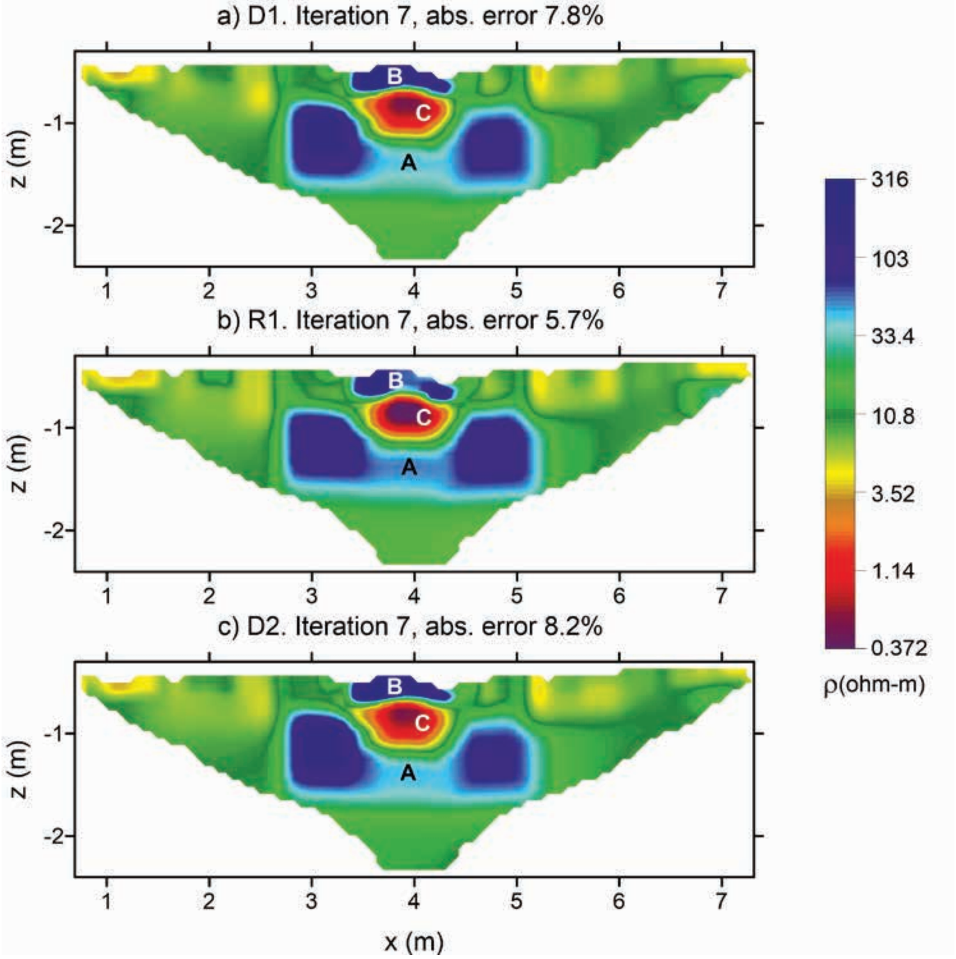

Figure 4 The 2D inversion results for Profile 1, obtained without considering the data errors, from the data (a) D1, (b) R1, and (c) D2.

to the right of the column. Once more, the alternative data error estimates (Figure 7b) present a positive correlation with the standard ones, although their mean and maximum values are lower, 14% and 50%, respectively.

As expected, when we performed the 2D inversion of each dataset D1, R1, and D2, without considering the data errors, the inversion errors remained high (e.g., 70%, 67%, and 75%, respectively, at the fifth iteration) and could not be reduced by further increasing the number of iterations. In addition, the three models obtained presented marked differences between them. This last point was central to confirming that a reliable characterisation of the subsoil had not been obtained.

We applied two different procedures to improve these results. The first one was to repeat the same type of inversions after removing from the datasets D1, R1, and D2 (each one consisting of 324 apparent resistivity values) those points with errors ρ (D1 & R1) greater than a given cut-off level. The optimum cut-off value was determined by trial and error. It was observed that, up to a certain point, by lowering the cut-off level, the convergence errors decreased and the similarities between the three resulting models increased, and beyond that point, the differences between these models tended to increase again, and an excessive smoothing of the anomalies was obtained, which indicated that valuable information about the

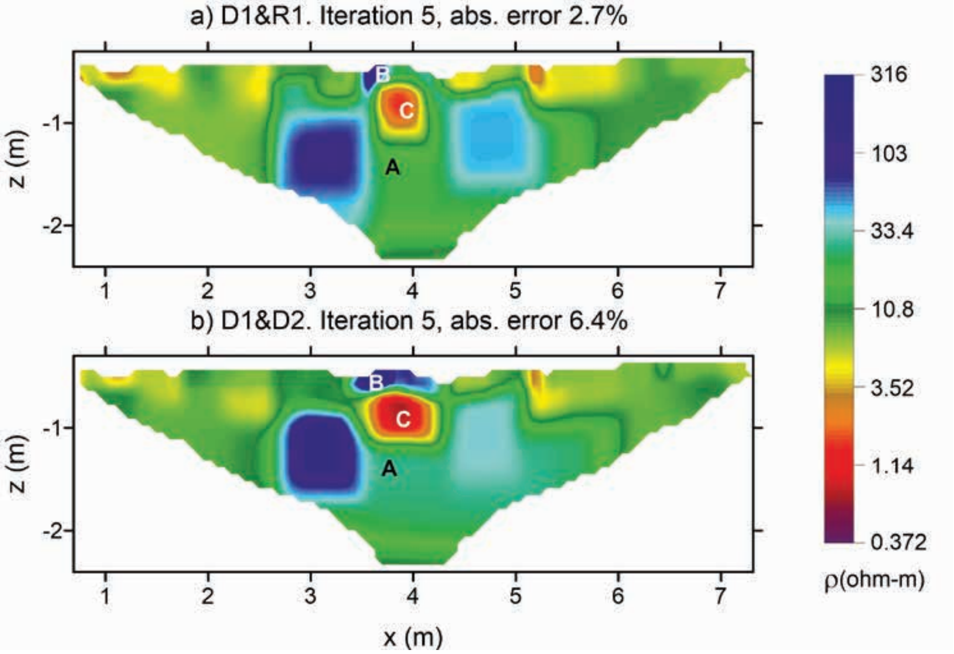

Figure 5 The 2D inversion results for Profile 1, obtained (a) from the data D1 & R1, defined by equation (1), considering the error estimations given by equation (3), and (b) from the data D1 & D2, defined by equation (2), considering the error estimations by equation (4).

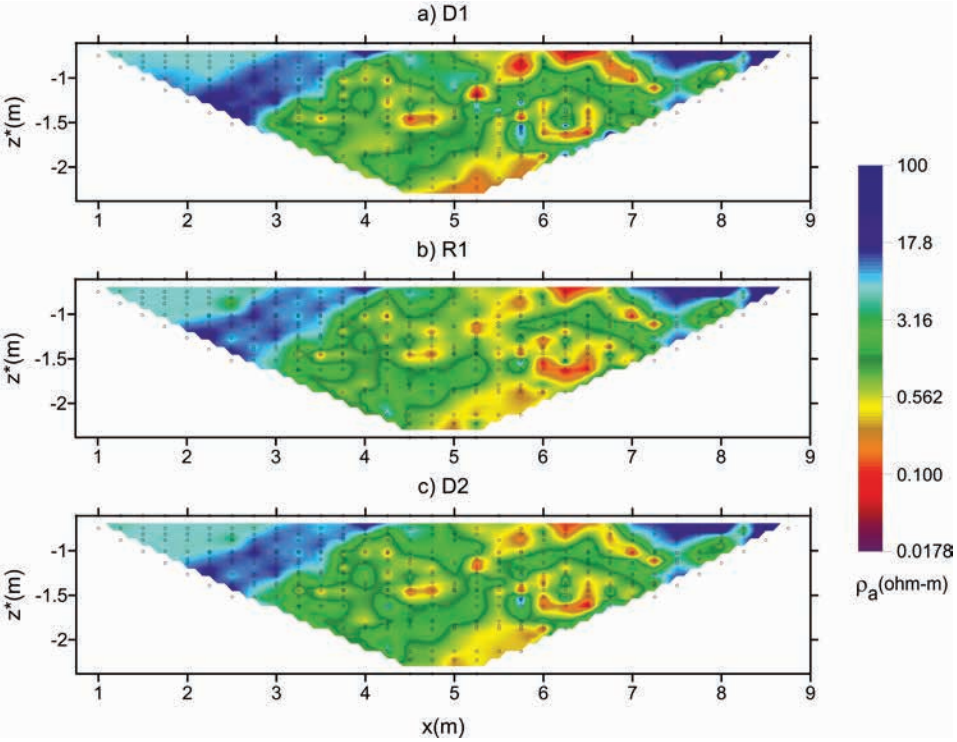

Figure 6 Apparent resistivity pseudosections corresponding to Profile 2 for (a) the first set of direct measurements (data D1), (b) the reciprocal measurements (data R1), and (c) the second set of direct measurements, performed after reinstalling the electrodes (data D2). Z* denotes the median depth of investigation.

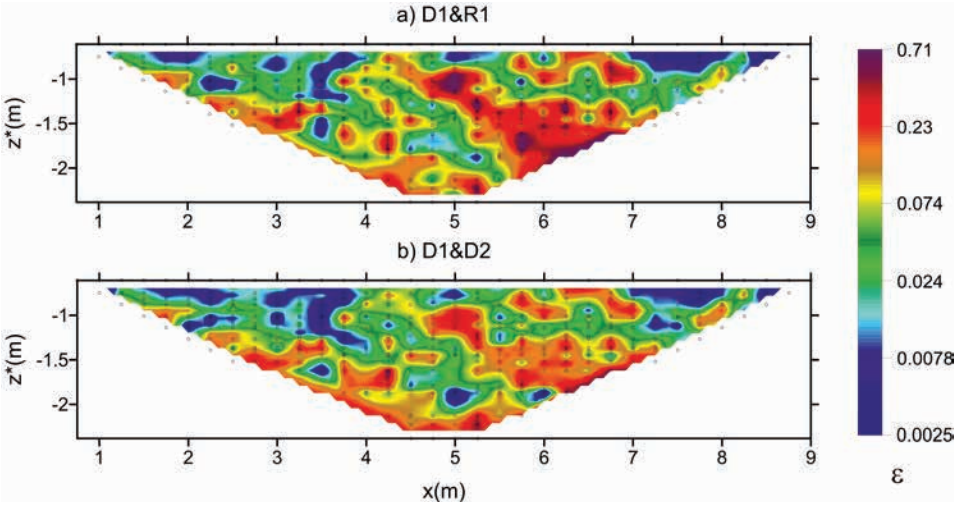

Figure 7 Pseudosections of unitless relative errors, ε, for Profile 2, calculated (a) from the data D1 and R1 through equation (5) and (b) from the data D1 and D2 through equation (6). Z* denotes the median depth of investigation.

target structures began to be lost. The resulting optimum cut-off value was 35%, and corresponded to eliminate 60 points from each dataset, obtaining reduced datasets (named D1a, R1a, and D2a). The convergence errors of the corresponding inversions were 38%, 33%, and 34%, respectively. Although the differences between the images were lower than in the previous case, they were still important.

The second procedure used to improve the results of the separate 2D inversions, made without considering data errors, provided better results. It is explained next. First, the data points that, in the original inversions of the complete datasets D1, R1, and D2, presented root mean square (RMS) fitting errors greater than 140% were removed from these datasets, and a second round of the same type of inversions was carried out. In total, 47 data points were removed from D1, 46 from R1, and 49 from D2, again obtaining reduced datasets (D1b, R1b, and D2b, respectively). The obtained convergence errors (35%, 37%, and 35%, respectively) were comparable with those obtained for D1a, R1a, and D2a, but the similarities between the resulting images were somewhat greater in this case. This procedure was applied once more, in this case removing 25, 40, and 31 data from D1b, R1b, and D2b, respectively, which presented RMS fitting errors greater than 90% in the second round of inversions. The corresponding datasets are respectively called D1c, R1c, and D2c. After this third round of inversions, the correlation between the models improved even more, and the convergence errors decreased again, up to values between 20% and 28%. These were the best solutions, since like that observed in the case of the first procedure, removing even more data led to a new increase in the differences between the models and to an excessive smoothing of the observed anomalies.

As examples, the ERTs corresponding to the inversions of D1c, R1c, and D2c are shown in Figure 8(a–c), respectively. As a whole, these models have certain similarities with those obtained for Profile 1 (Figures 4 and 5) and several differences. Below an upper resistive cover (anomaly D) there is a very conductive anomaly (anomaly E), with a width of about 1 m and located approximately between $x = 4.2$ m and 5.2 m and depths 0.9–1.6 m. There is also a resistive block to the left of the profile (anomaly FL), but it is not possible to detect its full dimension. Another resistive anomaly appears to the right of the profile (FR), but with lower resistivity and extension than FL. It seems to be distorted by the presence of a second very conductive anomaly beginning at a depth of about 2 m (anomaly G2). Analogously, the anomaly D associated with the upper resistive material appears very well-delineated to the left of the column, extending up to $x = 3.6$ m and $z = -0.9$ m, and is much more distorted to the right, partly by the anomaly G1. It is important to take into account that, in general, the resolution is probably lower in the right part of the models, where more data points had to be removed in the first and second procedures used for improving the inversion results, due to their high standard errors or high RMS fitting errors, respectively. For these reasons, even though the anomalies G1, G2, and FR appeared in the three models (Figure 8(a–c)), some of them could still be spurious. It is worthwhile to note that the deployment of longer profiles or the complementary use of a more robust configuration such as the Wenner-α array could have helped elucidate this. However, this could not be done due to the spatial limitations previously mentioned.

We then performed 2D inversions of the data D1 & R1 (equation (1)) and D1 & D2 (equation (2)), using the error estimations via equations (3) and (4), respectively. Even though we did not remove any data from these datasets, the convergence errors decreased to 14% and 21%, respectively. Like for Profile 1, the two obtained models were similar, although they had differences somewhat greater than the models in Figure 5(a,b). The ERT corresponding to the inversion of D1 & R1 is shown, as an example, in Figure 8d. Again, contrary to what could have been expected, this model that has a lower convergence error also has a lower resolution. The main anomalies present in Figure 8(a–c) are still evidenced, but with less contrasting resistivity values and worse-delineated contours.

Profile 3

Finally, we analyse Profile 3. The column corresponding to this profile had the same dimensions as the one in Profile 1 and was also centred at $x = 4$ m. In this case, we did not have to apply any topographical corrections. Figure 9(a,b) shows the pseudosections of the standard and alternative relative error estimations for the data of this profile, obtained using equations (5) and (6), respectively. As it can be appreciated by comparing Figure 9a with Figures 3a and 7a, data quality was much better than in the previous case (Figure 7a) but not as good as in the case of Profile 1 (Figure 3a). The mean and maximum values of data errors were 3.5% and 7%. Again, the alternative errors had a positive correlation with the standard ones, although with lower overall values (mean: 2.1%; maximum: 5%).

The results of the 2D inversions of the data D1, R1, and D2, performed without including any information about data errors, are shown in Figure 10(a–c), respectively. A similarity can be appreciated between these results and the ones corresponding to Profile 1 (Figure 4(a–c)). A resistive structure is also found (anomaly H), with similar dimensions (approximately 2.6-m wide and 0.8-m thick) and resistivity values as anomaly A, which also contains two more resistive zones. In this case, this structure

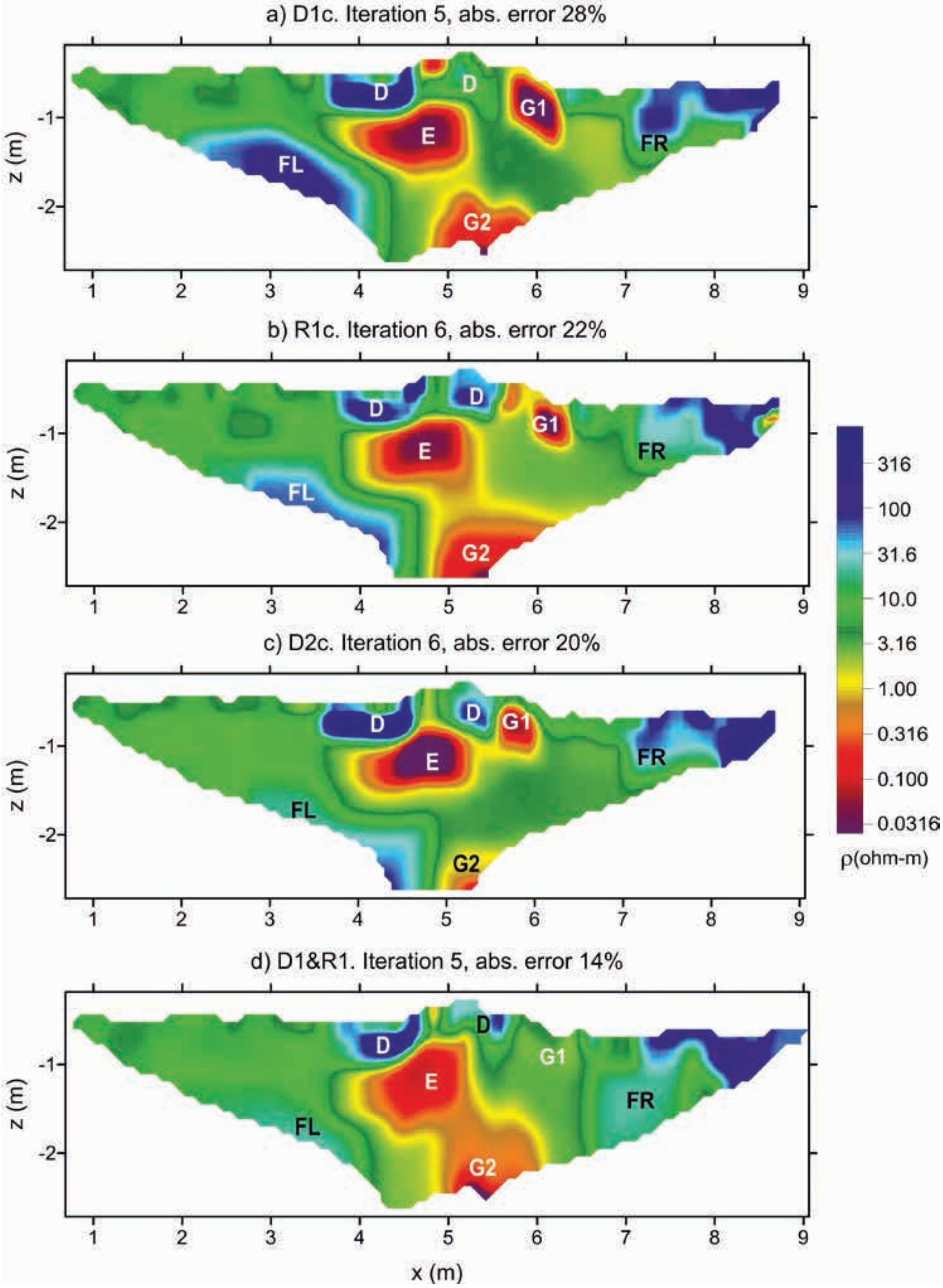

Figure 8 The 2D inversion results for Profile 2. (a–c) Models obtained without considering the data errors, from data D1c, R1c, and D2c (see the text for a detailed description regarding these datasets were obtained). (d) Model obtained from the data D1 & R1, defined by equation (1), considering the error estimations given by equation (3).

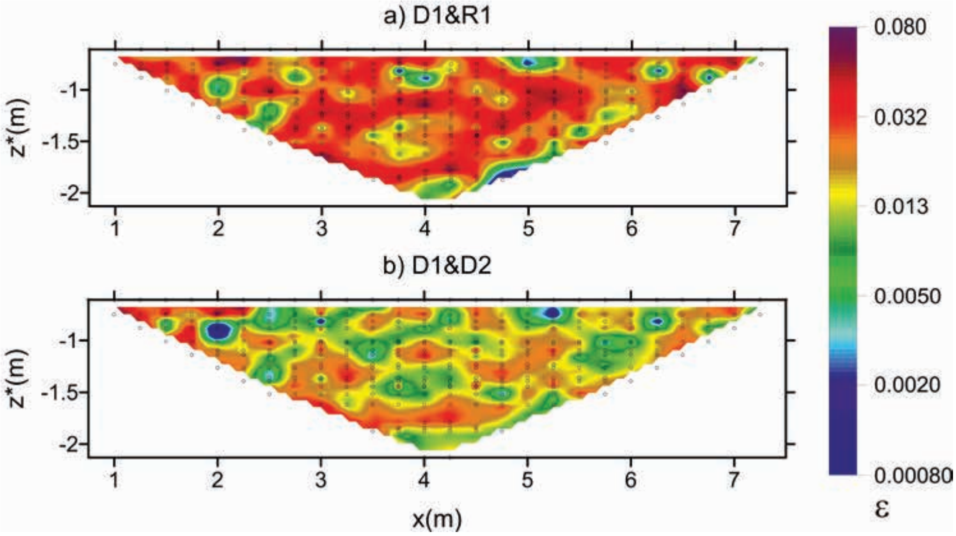

Figure 9 Pseudosections of unitless relative errors, ε, for Profile 3, calculated (a) from the data D1 and R1 through equation (5), and (b) from the data D1 and D2 through equation (6). Z* denotes the median depth of investigation.

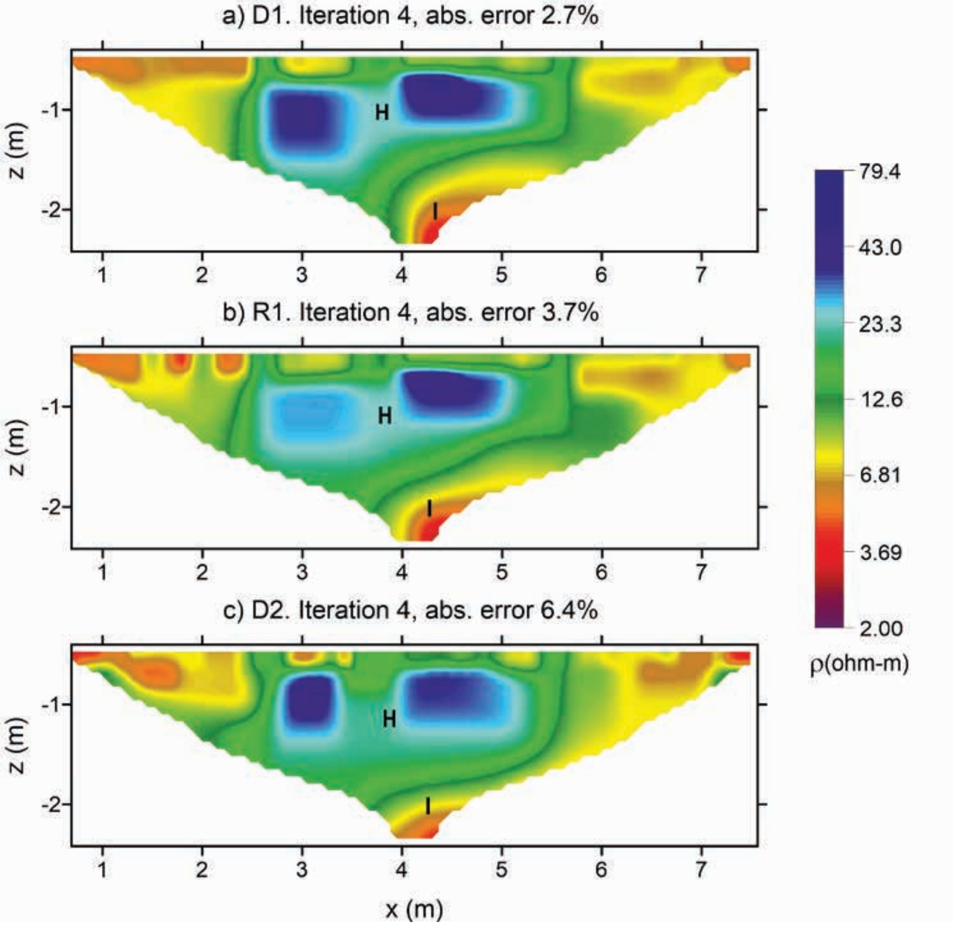

Figure 10 The 2D inversion results for Profile 3. (a–c) Models obtained from datasets D1, R1, and D2, respectively, without considering data errors.

is located between the depths 0.7 m and 1.5 m. The main differences with respect to the results of Profile 1 are the absence of a central conductive anomaly, and that the upper cover material is mostly conductive instead of resistive (although a slight increase in resistivity is observed near the actual lateral position of the column). Another relevant feature is that to the left of $x = 4$ m, at a depth of about 2 m, a conductive area appears (anomaly I) that distorts the shape of the resistive structure H. This is similar to that observed for the anomalies FR and G2 in the ERTs corresponding to Profile 2.

In general, the conductivity contrasts and the delineation of the shape of the main anomalies are worse in the models in Figure 10(a–c) than they are in the respective models in Figure 4(a–c). This could be due to the somewhat higher data error levels obtained for this profile, in comparison with Profile 1. Once more, the models in Figure 10, which have less resolution, present lower convergence errors (2.7%, 3.7%, and 6.4%, respectively) than the ones in Figure 4 (7.8%, 5.7%, and 8.2%, respectively).

The 2D inversion results for the datasets D1 & R1 and D1 & D2, obtained from equations (1) and (2), respectively, and performed considering the errors in equations (3) and (4), are shown in Figure 11(a,b). Like it occurred for the two former profiles, convergence errors (2.2% and 2.8%, respectively) were reduced with respect to the values obtained for the inversions performed without considering the data errors, but at the same time, the quality of the images decreased to a great extent, especially in the case corresponding to the inversion of D1 & R1.

Summarising, considering the inversion results obtained for Profiles 1 and 3 (Figures 4 and 5, and Figures 10 and 11, respectively), we interpret that the observed resistive structures A and H, about 2.6-m wide and 0.8-m thick, correspond to the bases of the columns, made of concrete. In the case of Profile 2 (Figure 8), only some of the features of the base could be detected; it seems to be composed of a central conductive zone, about 2-m wide, and two resistive areas at both sides (FL and FR) that may continue outside the modeled region. Other characteristics of the ERTs were more difficult to interpret. On one side, a localised conductive anomaly is detected near the actual position of the metallic column in the cases of Profiles 1 and 2 (anomalies C and E, respectively), but not in the case of Profile 3. In addition, the material above anomalies C and E is resistive (anomalies B and D, respectively), whereas in the case of Profile 3, this zone is mostly conductive, with the sole exception of a slight increase in resistivity near the actual position of the column. Finally, the resistive anomalies A and H associated to the bases of the columns in Profiles 1 and 3, respectively, present analogous and more resistive areas towards the sides, when their resistivities were expected to be more uniform.

Given the space constraints for the measurements, it was not possible to make a 2D grid around each column or, at least, several profiles in two perpendicular directions. Therefore, to refine the interpretation and try to elucidate the described features of the 2D ERTs, we performed numerical simulation experiments, combining 3D forward modelling with 2D inversions. The results are presented next.

NUMERICAL SIMULATIONS

The 3D forward modelling and 2D inversions were performed using the codes Res3Dmodx64 version 3.05 and Res2Dinvx64 version 4.05, respectively (Geotomo Software; Loke and Barker 1996a,b).

The 3D models used to represent the studied type of structures, in which general characteristics were known, are like the one shown in Figure 12. Figure 12a shows a vertical section that passes through the center of this model. As it can be observed, first, there is an upper conducting layer with a thickness of 1 cm, representing the metallic cover of the floor and then a resistive layer representing the concrete layer, indicated in grey. The metallic column is joined at its bottom with a square anchor plate which is also metallic; these structures are indicated in red. They are embedded in a base consisting of a rectangular cuboid of

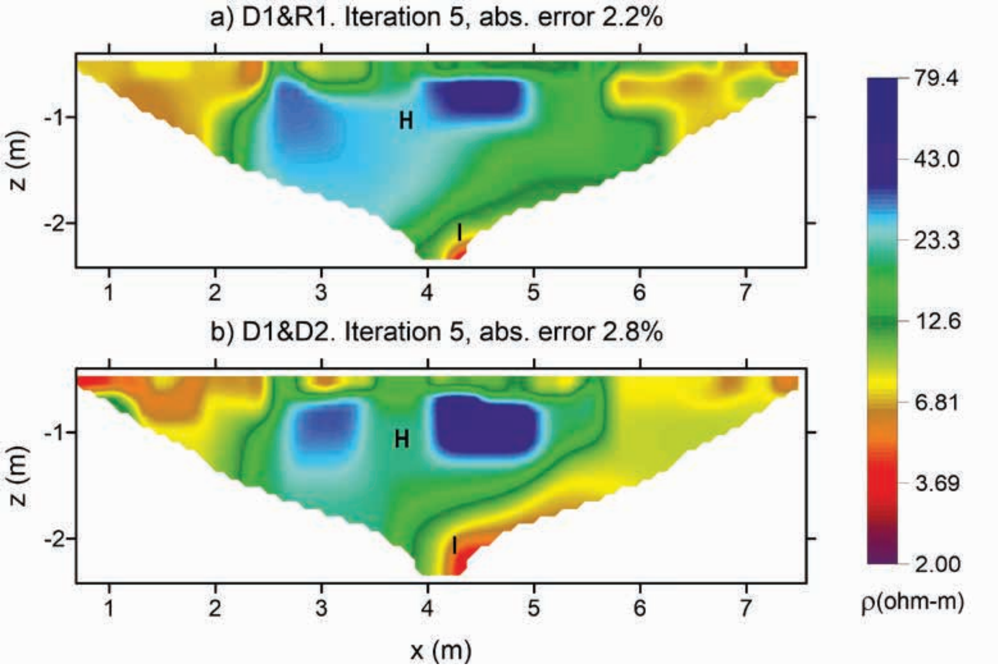

Figure 11 The 2D inversion results for Profile 3, obtained (a) from data D1 & R, defined by equation (1), considering the error estimations given by equation (3) and, (b) from data D1 & D2, defined by equation (2), considering the error estimates from equation (4).

concrete, shown in blue. Finally, the part of the column outside the base is separated from the background through a cover of thickness *c*, also made of concrete (again indicated in blue). The dimensions assigned to the described structures are marked in the figure. Figure 12b shows a 3D view of the model below the depth of 31 cm. This is the depth at which the electrodes are placed, where the concrete layer ends.

The electrical resistivity values assigned to the described structures were 0.5 Ωm for the column, anchor plate and upper layer; 100 Ωm for the column base, the column covering, and the concrete layer; and 5 Ωm for the host medium/soil, respectively.

The values of the parameters were selected based on prior knowledge about the general characteristics of the column bases and on the main features observed in the 2D ERTs corresponding to the experimental Profiles 1 and 3. The resistivity of the metallic structures was chosen low enough to obtain insightful results, but high enough to not destabilise the numerical calculations. The thickness of the cover of the column, *c*, was varied to investigate if some of the differences between the results obtained for the three profiles could be reproduced. The model shown in Figure 12(a,b) corresponds to c = 0.125 m (Model 1), whereas Models 2 and 3 correspond, respectively, to c = 0.25 m and 0.375 m. A cut of these models at z = −0.31 m is shown in Figure 12c.

The finite difference mesh used for the 3D forward modelling computations consisted of 64 × 64 × 32 cubic elements of 0.125-m side, in the volume x = 0–8 m, y = 0–8 m, z = 0 to −4 m. As the main goal of the simulations was to aid in the interpretation of the results of the survey, for each 3D model, we calculated the synthetic apparent resistivities for a dipole–dipole line in the *x*-direction, which is 8-m long, with electrode spacings a = 0.25 m, 0.5 m, 0.75 m, 1 m and 1.25 m, and dipole separation factors up to n = 8, located 0.25 m away from the center of the column at a depth of 0.31 cm, which is similar to the configuration and location of the actual survey profiles. As can be observed in Figure 12c, the three proposed models recreate three different possible positions of the profile with respect to the column covering.

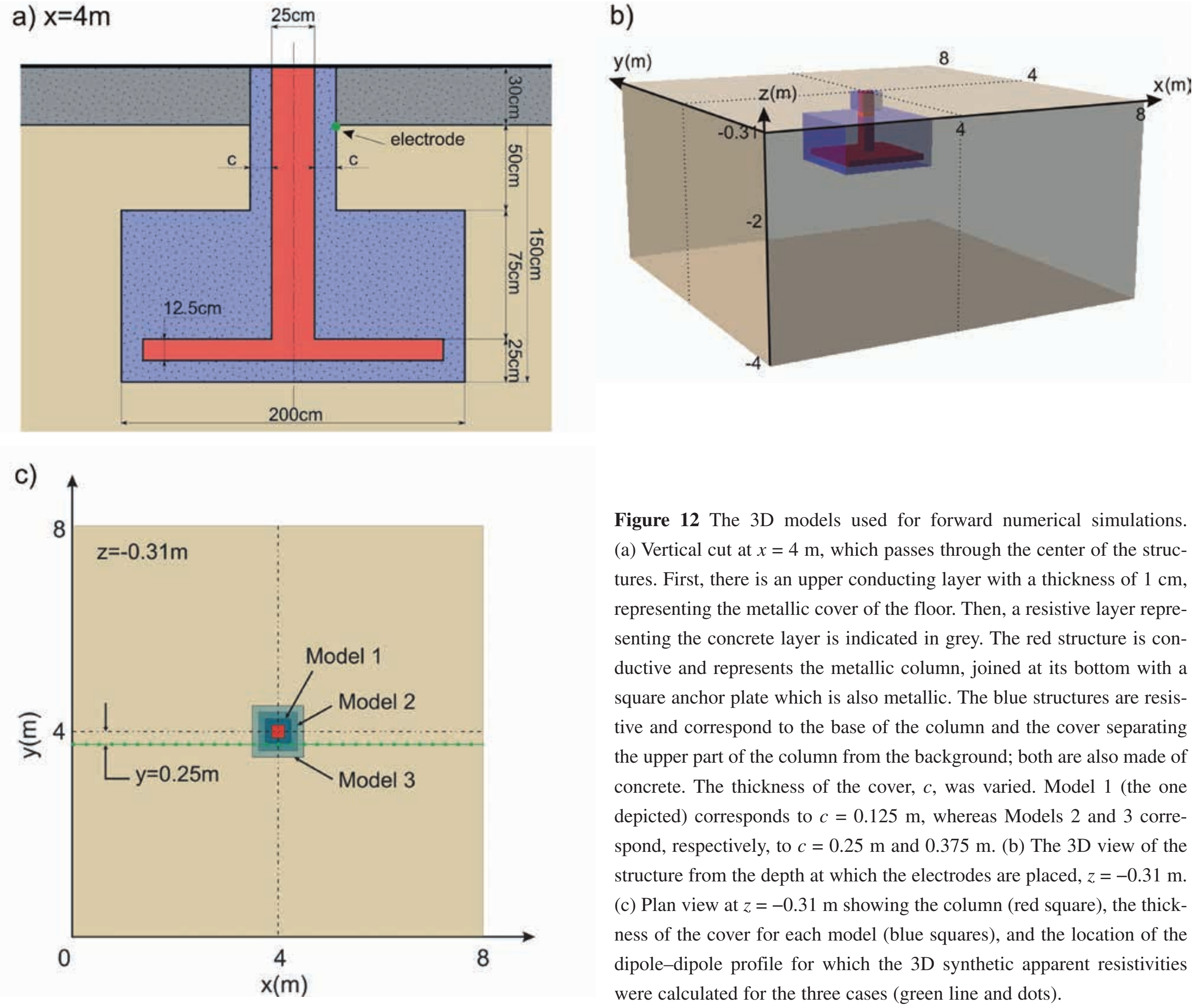

Figure 12 The 3D models used for forward numerical simulations. (a) Vertical cut at x = 4 m, which passes through the center of the structures. First, there is an upper conducting layer with a thickness of 1 cm, representing the metallic cover of the floor. Then, a resistive layer representing the concrete layer is indicated in grey. The red structure is conductive and represents the metallic column, joined at its bottom with a square anchor plate which is also metallic. The blue structures are resistive and correspond to the base of the column and the cover separating the upper part of the column from the background; both are also made of concrete. The thickness of the cover, *c*, was varied. Model 1 (the one depicted) corresponds to c = 0.125 m, whereas Models 2 and 3 correspond, respectively, to c = 0.25 m and 0.375 m. (b) The 3D view of the structure from the depth at which the electrodes are placed, z = −0.31 m. (c) Plan view at z = −0.31 m showing the column (red square), the thickness of the cover for each model (blue squares), and the location of the dipole–dipole profile for which the 3D synthetic apparent resistivities were calculated for the three cases (green line and dots).

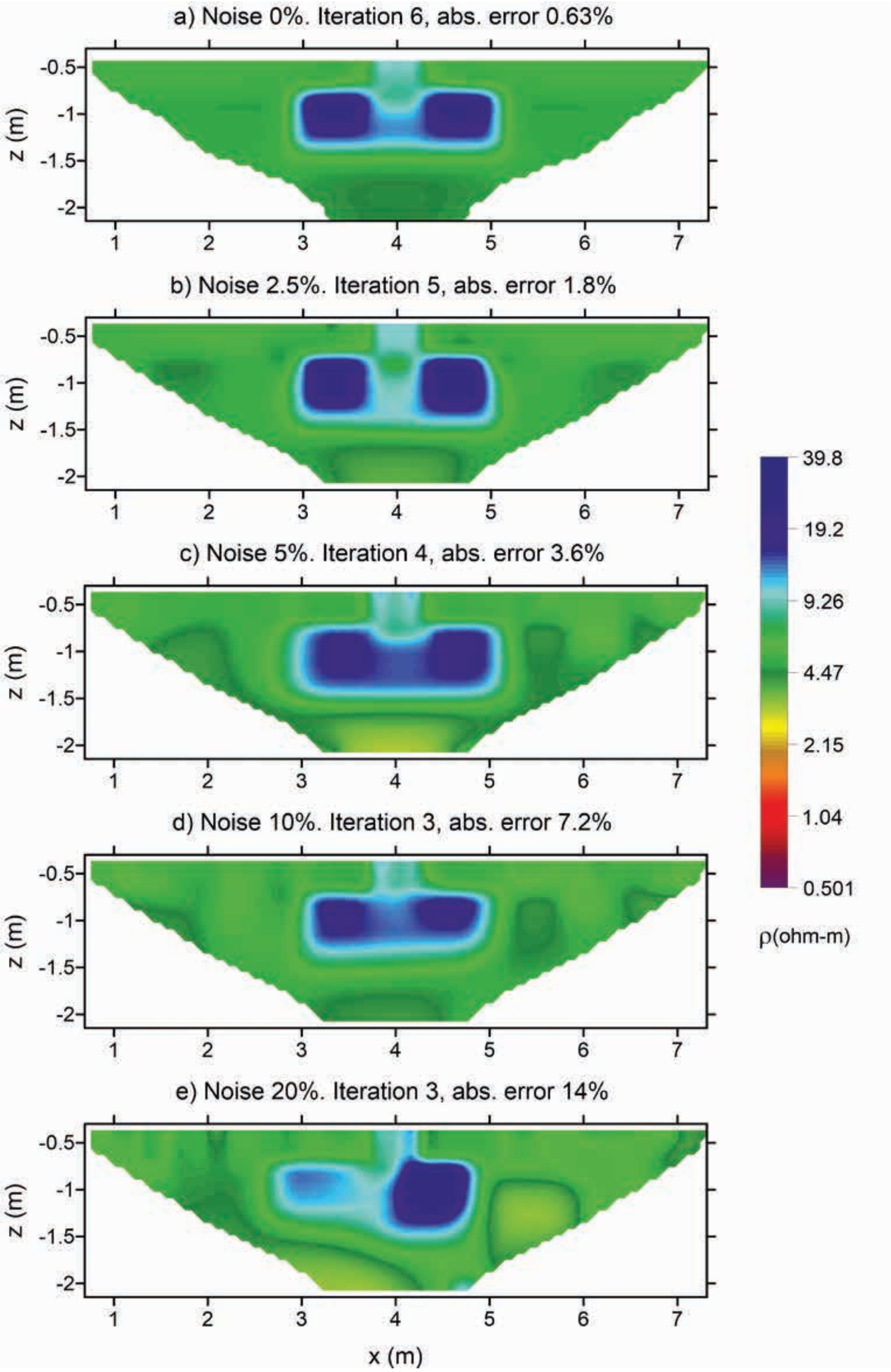

Figure 13 Results of 2D inversion of the 3D synthetic data of Model 1 (column cover thickness $c = 0.125$m) corresponding to the dipole–dipole line; the location is shown in Figure 12c. Different levels of Gaussian noise were added to these data before the 2D inversion: (a) 0%, (b) 2.5%, (c) 5%, (d) 10%, and (e) 20%. No prior information about the data errors was provided in inversion.

Before performing the 2D inversions, different levels of Gaussian noise were added to the synthetic 3D data, in order to represent different possible acquisition conditions. As the best results for the survey profiles corresponded to 2D inversions performed without considering the data errors, we also inverted these synthetic profiles without considering them, in order to compare the obtained results under the same conditions.

Figures 13–15 show the resulting images for Models 1–3, including different Gaussian errors, respectively. These results allow us to explain most of the main features observed in the 2D

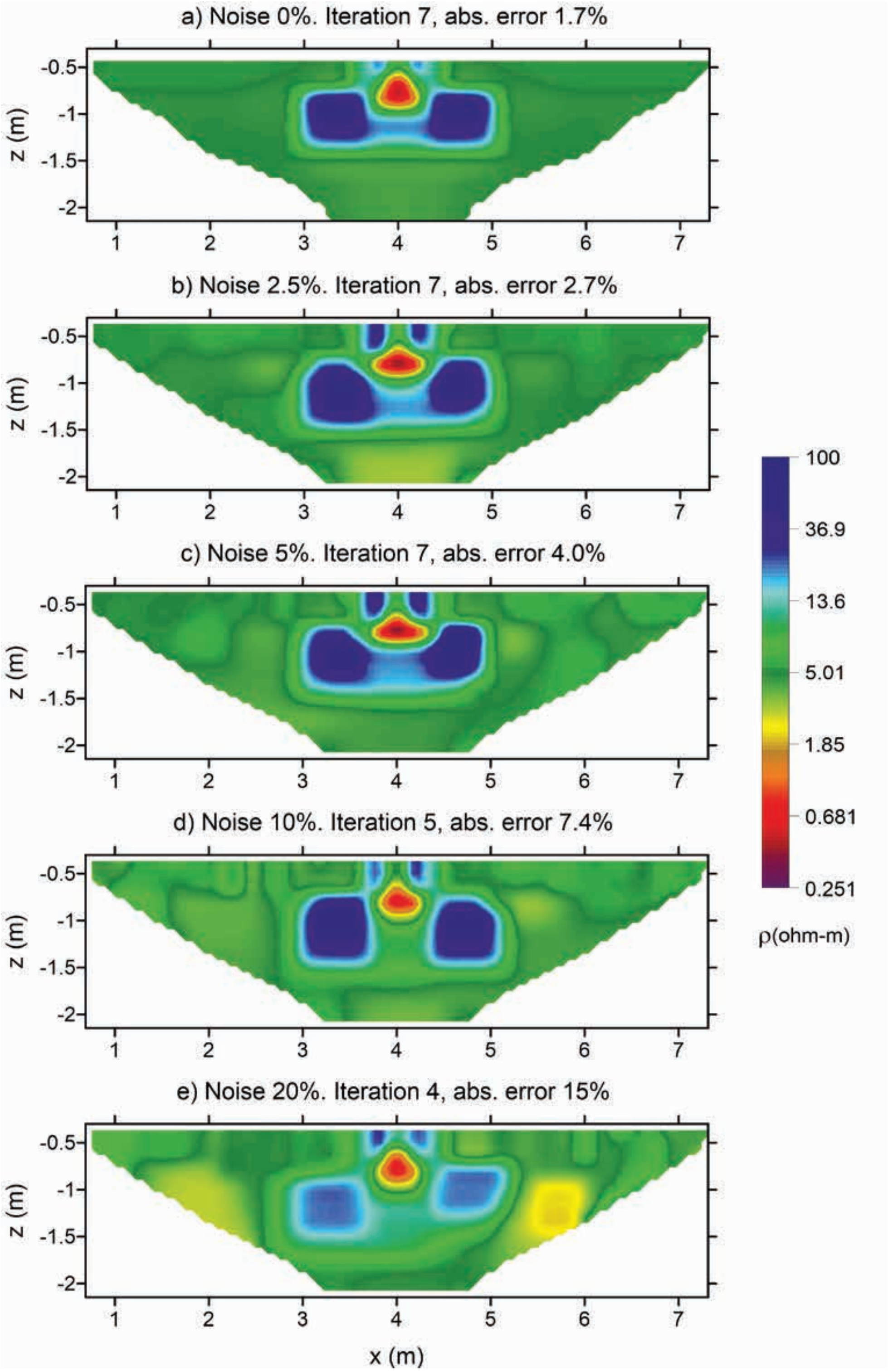

Figure 14 Results of 2D inversion of the 3D synthetic data of Model 2 (column cover thickness c = 0.25m) corresponding to the dipole–dipole line; the location is shown in Figure 12c. Different levels of Gaussian noise were added to these data before the 2D inversions: (a) 0%, (b) 2.5%, (c) 5%, (d) 10%, and (e) 20%. No prior information about the data errors was provided in inversion.

images corresponding to the experimental profiles, since the models in Figure 13 resemble the 2D ERTs obtained for Profile 3 (Figures 10 and 11), whereas the ones in Figures 14 and 15 are similar to those corresponding to Profile 1 (Figures 4 and 5) and, to a lesser extent, to those of Profile 2 (Figure 8). In particular, in the models of Figure 13, there is no central highly conductive anomaly; in addition, the resistivity above the base is that of the host medium, except for a moderate resistivity increase around x = 4 m. Both results are similar to that observed in Figure 10. On the other hand, the models shown in Figures 14 and 15 exhibit a marked central conductive anomaly (similar to anomalies C in Figures 4 and 5, and E in Figure 8), accompanied by an upper resistive anomaly (analogous anomalies B in Figures 4 and 5, and D in Figure 8); these anomalies are wider and more pronounced in the case of Model 3.

The origin of the described differences can be understood taking into account that the position of the synthetic profile with respect to the column cover is different among Models 1–3 (Figure 12c). In the case of Model 1, the profile is located on the border between the conductive host medium and the resistive column cover; then, most

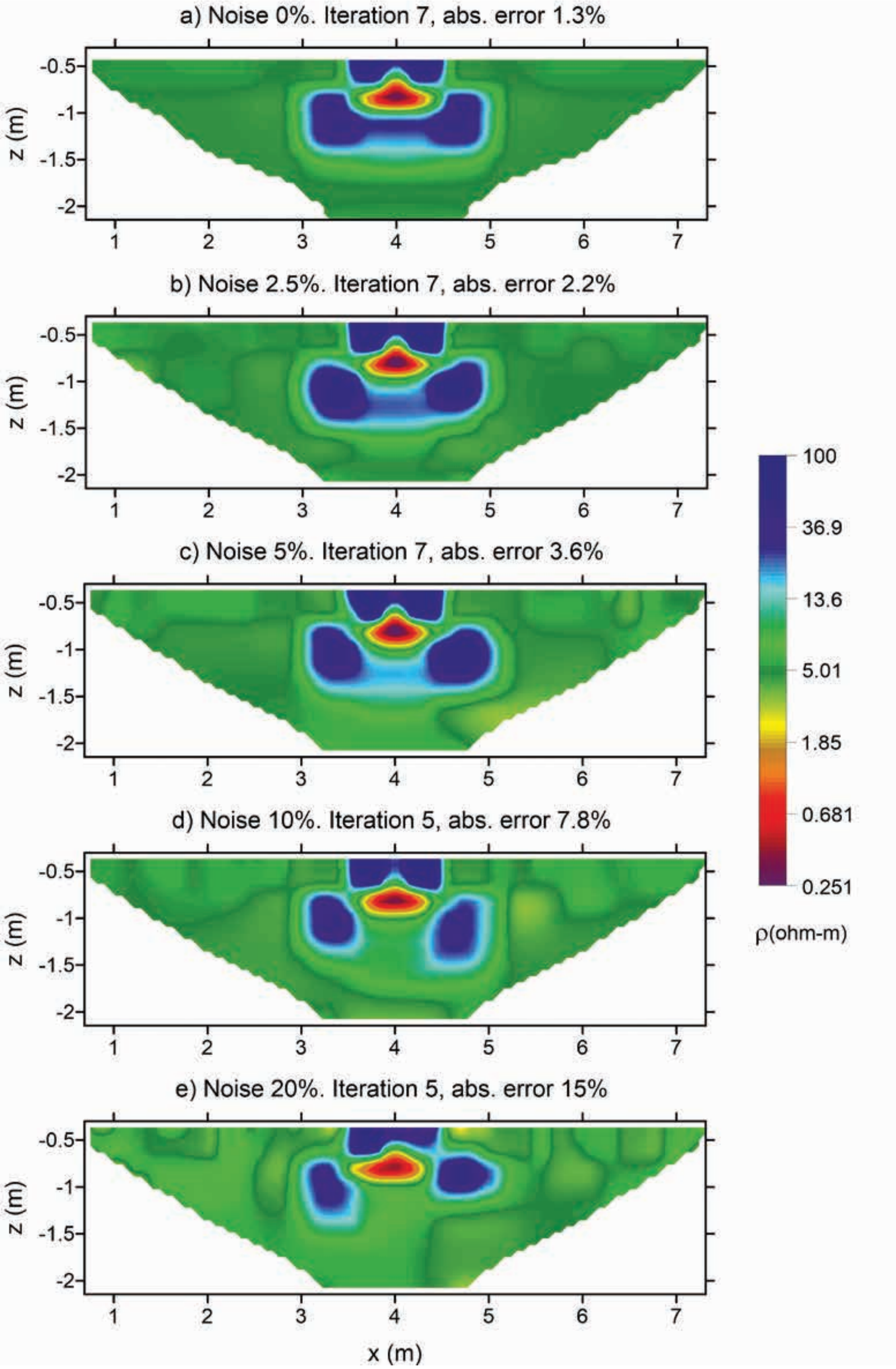

Figure 15 Results of 2D inversion of the 3D synthetic data of Model 3 (column cover thickness $c = 0.375$m) corresponding to the dipole–dipole line; the location is shown in Figure 12c. Different levels of Gaussian noise were added to these data before the 2D inversions: (a) 0%, (b) 2.5%, (c) 5%, (d) 10%, and (e) 20%. No prior information about the data errors was provided in inversion.

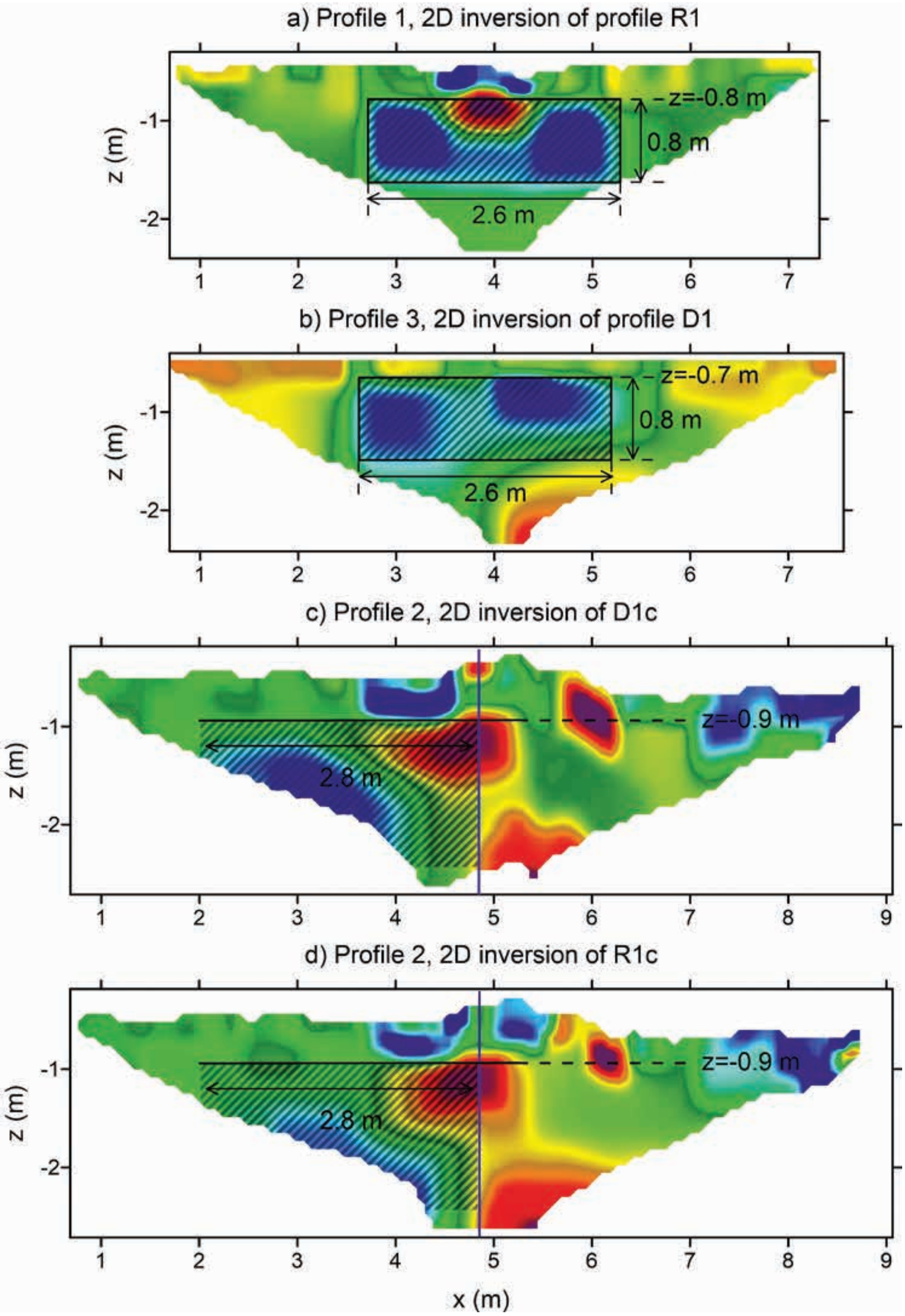

Figure 16 Summary of the results of the study, based on the best models obtained for each profile. The shadowed zones in the images indicate the areas associated with the bases of the columns. In the case of column 2, centred at x = 4.8 m, the base is only partially observable. As data errors were high for this column, only the depth to the top of the base and a very approximate value of its half-width could be established; the location of its bottom remains undetermined.

of the current flows through the soil, and only a small amount of current passes through the cover. On the other hand, in the case of Model 2, the profile passes over the column cover. Therefore, part of the current flows through this structure, another part goes to the ground, and another one reaches the metal column and its anchor plate. Finally, for Model 3, the profile also crosses over the column cover but makes it farther from the ground than in the case of Model 2; as a result, more current flows through the cover, the column, and its anchoring, and less goes to the ground.

Regarding the anomalies associated to the bases of the columns, even when no noise is added to the synthetic data, the images always exhibit two more resistive regions (Figures 13a, 14a, and 15a). This 3D effect can be clearly appreciated in the 2D ERTs corresponding to Profiles 1 and 3 (anomalies A and H,in Figures 4 and 5 and in Figures 10 and 11, respectively). As the noise level increases, the resolution decreases for the three models (Figures 13–15, b–e); the structure of the base becomes less well defined, and asymmetries begin to appear in the shape and resistivity on both sides. In addition, in the case of Models 2 and 3 (Figures 14 and 15 b–e, respectively), the part of the base below the conductive body becomes less resistive, even up to the point of being almost indistinguishable from the host medium in some of the examples (Figures 14d, 15d, and 15e). Considering the high error level in the data corresponding to Profile 2, this effect, superimposed on the distortion introduced by the highly conductive body G2, provides a plausible explanation as to why a wide conductive zone is detected in the central part of the base of this column. Finally, in the case of the anomaly H, corresponding to the base of column 3 (Figures 10 and 11), the described type of asymmetries is superimposed on the distortion produced by the conductive structure I.

DISCUSSION

As stated previously, the general characteristics of the targets were known, and we used this knowledge to analyse the inversion results.

For Profile 1, the 2D ERTs obtained from the inversion of the data D1, R1, and D2, made without considering the data errors, present similar features, which are in agreement with the expected characteristics. The errors of these inversions were reasonably low (between 5.7% and 8.2%), considering the site characteristics and the subsoil complexity. When datasets D1 & R1 and D1 & D2 (obtained by combining the data from profiles D1 and R1, and D1 and D2, respectively) were inverted, considering their corresponding error estimations, convergence errors decreased to 2.7% and 6.4%, respectively. However, the contours of the structures appeared less defined, and the resistivity contrasts were smaller.

Profile 3 exhibited a similar behavior. The models from the inversions of the three datasets D1, R1, and D2 resemble each other but are less than those obtained for Profile 1. The shape and the resistivity of the base are worse-defined in comparison with that case. Convergence errors were between 2.7% and 6.4%, for the inversions of D1, R1, and D2, respectively, and decreased to 2.2% and 2.8%, respectively, for the inversions of the combined data D1 & R1 and D1 & D2. Again, although the last two inversions have lower convergence errors, the models have less resolution (the worst results for the inversion of D1 & R1).

Comparing the results obtained for both profiles, it can be noted that the shape and the resistivity value of the base were worse-defined in the images corresponding to Profile 3. The data errors for this profile (see Figure 9) were greater than those corresponding to Profile 1 (see Figure 3). With the numerical simulations, we could determine that the lower resolution and part of the asymmetries observed in the images corresponding to Profile 3 are effects due to the noise in the data. Another important point that could be explained was why a localised conductive anomaly was observed in the central part of the ERTs corresponding to Profile 1, but it was not detected for Profile 3. According to synthetic modelling, this would be a consequence of the different location of the survey profile with respect to the column cover in each case. In addition, the two symmetric and more resistive zones observed in the anomalies associated to the bases of the columns in Profiles 1 and 3, were recognised as 3D effects.

The data corresponding to Profile 2 presented the highest error levels. Consequently, the errors of the inversion of the data D1, R1, and D2 were very high (between 67% and 75%), and the differences between the resulting models were large.

To improve the results of the inversions, we applied two different procedures. The first one was to remove from each dataset those points with errors ρ(D1 & R1) greater than a given cut-off level. The optimum cut-off value was 35%, which reduced the convergence errors of the corresponding inversions to values between 33% and 38%. Although the differences between the images were lower than those in the previous case, they were still important. In the second approach, we made successive inversions of D1, R1, and D2. In each case, the data with the highest fitting errors in the previous inversion were removed from the corresponding dataset before carrying out a new inversion. This procedure allowed us to reduce convergence errors to values between 20% and 28% and provided the best final models. Clearly, both procedures must be applied with caution, in order to avoid eliminating relevant information.

For the datasets D1 & R1 and D1 & D2, even without removing any data, the errors of the inversions decreased to 14% and 21%, respectively. Nevertheless, once again, the quality of these images was inferior.

In Figure 16, we summarise the results of the study, wherein the goal was to determine the depths and the approximate dimension of the column bases. The images shown are the ones that best resemble the actual structures, based on the analysis of the obtained results, including the numerical simulations. In the case of Profile 1, the inversion of data D1, R1, and D2 provided very similar results. Among them, for an illustration, we selected the image corresponding to the inversion of data D1. In the case of Profile 3, the three images, corresponding to the inversion of D1, R1, and D2, exhibit a distortion caused by the presence of the conductive body I, superimposed on the asymmetries due to the data errors, according to the results of the numerical modelling. The distortions caused by the conductive body are similar in these images. However, the effect of the errors seems to be lesser in the case of the inversion of D1. This is the reason why we selected this image for the final interpretation. Regarding Profile 2, even the best images, shown in Figure 8(a,b), presented some differences. We used both models to perform the interpretation. Taking into account that the data from the right part of the profile had larger errors and that, in this zone, the results were also affected by the presence of conductive bodies close to the base, we based our interpretation mainly on the left part of the images. We could clearly determine the depth to the top of the base. On the other hand, the base of the column was only partially observable. Therefore, as the length of this profile could not be extended, we only obtained a very approximate estimation of its minimum half-width, while its bottom could not be identified.

CONCLUSIONS

The objective of this work was to characterise the bases of columns located in a place with limited available space for the deployment of sensors and with other environmental constraints, such as high electromagnetic noise level, soil vibrations due to operating machines, and complex soil composition. In this context, we tested different strategies for both the acquisition and processing of geoelectric data, in order to determine which procedures would allow us to obtain more reliable results.

For each column, we acquired three sets of dipole–dipole datasets (a direct measurement, a reciprocal one, and a second direct measurement after removing and reinstalling the electrodes). In this way, we could estimate data errors. To analyse the results, we have taken into account the knowledge we had in advance about the main characteristics of the structures. In the ERT images, we expected to find structures with relatively high resistivity contrasts and well-defined geometric shapes.

According to the obtained results, the first conclusion is that, at least for this type of structures and with the inversion software used, inverting each dataset without considering the data errors provides more realistic images, even when the convergence errors are larger than the values obtained when the inversions are performed considering the data errors. This could be because the requirements on the fitting were reduced, which led to smoother models with a loss of resolution.

However, although the best results are obtained by inverting without considering the errors, it is still fundamental to have different sets of data, including the second direct measurements, to compare the images obtained in each case. This allows evaluating their degree of reliability and discard possible artefacts. This is especially important when the data errors are high.

In the case that the data errors are particularly high, the way to improve the inversion is either to eliminate the data with errors greater than a certain cut-off level or, through successive inversions, to eliminate the data whose fitting error exceeds a given cut-off level. To find the optimal cut-off for each procedure without losing relevant information, it is clearly necessary to have more than one set of data. In our particular case, the second procedure gave the best results; however, this may not always be the case.

Finally, numerical simulations, performed by combining 3D forward modelling with 2D inversions, allow for a more rigorous interpretation of the observed anomalies and aid in identifying the models that best define the target structures. Also, the synthetic results contribute to understand the effect of data errors in the quality of the images.

ACKNOWLEDGEMENTS

This work was partially supported by ANPCyT-PICT 2014-1613 and CONICET.

BIBLIOGRAPHY

Arjwech P., Everett M.E., Briaud J.-L., Hurlebaus S., Medina-Cetina Z., Tucker S. *et al.* 2013. Electrical resistivity imaging of unknown bridge foundations. *Near Surface Geophysics* **11**(6), 591–598.

Bonomo N., Osella A., Martinelli P., de la Vega M., Cocco G., Letieri F. *et al.* 2012. Location and characterization of the Sancti Spiritus Fort from geophysical investigations. *Journal of Applied Geophysics* **83**, 57–64.

Dabas M., Camerlynck C., Freixas I. and Camps P. 2000. Simultaneous use of electrostatic quadrupole and GPR in urban context: investigations of the basement of the Cathedral of Girona (Catalunya, Spain). *Geophysics* **65**(2), 526–532.

Dahlin T. and Zhou B. 2004. A numerical comparison of 2D resistivity imaging with 10 electrode arrays. *Geophysical Prospecting* **52**(5), 379–398.

Drahor M.G. 2011. A review of integrated geophysical investigations from archaeological and cultural sites under encroaching urbanization in İzmir, Turkey. *Physics and Chemistry of the Earth* **36**(16), 1294–1309.

Edwards L.S. 1977. A modeled pseudosection for resistivity and IP. *Geophysics* **42**(5), 1020–1036.

Eppelbaum L.V. 2011. Study of magnetic anomalies over archaeological targets in urban environments. *Physics and Chemistry of the Earth* **36**(16), 1318–1330.

Karhunen K., Seppänen A., Lehikoinen A., Monteiro P.J.M. and Kaipio J.P. 2010. Electrical resistance tomography imaging of concrete. *Cement and Concrete Research* **40**(1), 137–145.

Leucci G. and Negri S. 2006. Use of ground penetrating radar to map subsurface archaeological features in an urban area. *Journal of Archaeological Science* **33**(4), 502–512.

Loke M.H. and Barker R.D. 1996a. Rapid least-squares inversion of apparent resistivity pseudosections by a quasi-Newton method. *Geophysical Prospecting* **44**(1), 131–152.

Loke M.H. and Barker R.D. 1996b. Practical techniques for 3D resistivity surveys and data inversion. *Geophysical Prospecting* **44**(3), 499–523.

Loke M.H., Acworth I. and Dahlin T. 2003. A comparison of smooth and blocky inversion methods in 2D electrical imaging surveys. *Exploration Geophysics* **34**(3), 182–187.

Loke M.H., Chambers J.E., Rucker D.F., Kuras O. and Wilkinson P.B. 2013. Recent developments in the direct-current geoelectrical imaging method. *Journal of Applied Geophysics* **95**, 135–156.

Martorana R., Fiandaca G., Casas Ponsati A. and Cosentino P. L. 2009. Comparative tests on different multi-electrode arrays using models in near-surface geophysics. *Journal of Geophysics and Engineering* **6**(1**),** 1–20.

Niederleithinger E., Abraham O. and Mooney M. 2015. Geophysical methods in civil engineering: overview and new concepts. *International Symposium Non-Destructive Testing in Civil Engineering* (NDT-CE), Berlin, Germany, September 2015. Bundesanstalt für Materialforschung und-prüfung (BAM).

Osella A., Martinelli P., Grunhut V., de la Vega M., Bonomo N. and Weissel M. 2015. Electrical imaging for localizing historical tunnels at an urban environment. *Journal of Geophysics and Engineering* **12**(4), 674–685.

Papadopoulos N., Sarris A., Yi M.-J. and Kim J.-H. 2009. Urban archaeological investigations using surface 3D ground penetrating radar and electrical resistivity tomography methods. *Exploration Geophysics* **40**(1**),** 56–68.

Parasnis D.S. 1988. Reciprocity theorems in geoelectric and geoelectromagnetic work. *Geoexploration* **25**(3), 177–198.

Park S.K. and Van G.P. 1991. Inversion of pole-pole data for 3-D resistivity structure beneath arrays of electrodes. *Geophysics* **56**(7), 951–960.

Szalai S., Novák A. and Szarka L., 2011. Which geoelectric array sees the deepest in a noisy environment? Depth of detectability values of multielectrode systems for various 2D models. *Physics and Chemistry of the Earth* **36**(16), 1398–1404.

Szalai S., Koppan A., Szokoli K. and Szarka L. 2013. Geoelectric imaging properties of traditional arrays and of the optimized Stummer configuration. *Near Surface Geophysics* **11**, 51–62.

Szalai S., Lemperger I., Metwaly M., Kis Á., V. Wesztergom, Szokoli K. *et al*. 2014. Increasing the effectiveness of electrical resistivity tomography using Y_{11n} configurations. *Geophysical Prospecting* **63**(2), 508–524.

Tsokas G.N., Tsourlos P.I., Vargemezis G.N. and Pazaras N.T. 2011. Using surface and cross-hole resistivity tomography in an urban environment: an example of imaging the foundations of the ancient wall in Thessaloniki, North Greece. *Physics and Chemistry of the Earth* **36**(16)**,** 1310–1317.

Zhou B. and Dahlin T. 2003. Properties and effects of measurement errors on 2D resistivity imaging surveying. *Near Surface Geophysics* **1**(3)**,** 105–117.